

# Large Eddy Simulation of Separated Flow over a Two-dimensional Hump with and without Control by Means of a Synthetic Slot-jet

Alexandros Avdis · Sylvain Lardeau ·  
Michael Leschziner

Received: 30 September 2008 / Accepted: 15 April 2009 / Published online: 16 May 2009  
© Springer Science + Business Media B.V. 2009

**Abstract** Large Eddy Simulations for two flows separating from a two-dimensional hump in a duct are reported and discussed. The flows differ through the presence or absence of a synthetic slot-jet injected in a sinusoidal manner, i.e. at zero net mass-flow rate, close to the location of separation and intended to reduce (“control”) the extent of the separated region. Results reported include instantaneous visualisations, pre-multiplied spectra, wall-pressure distributions, streamfunction fields and profiles of velocity and second moments. For both flows, agreement between the simulations and the experimental results is generally good, especially in respect of the overall control effectiveness of the synthetic jet, despite the use of an approximate wall treatment bridging the viscous sublayer. Proper Orthogonal Decomposition of the velocity field is used to study structural features, and this shows that the most energetic mode in the base flow is representative of large streamwise vortices in the separated region, while in the controlled flow, most of the energetically dominant modes are associated with large spanwise vortices.

**Keywords** Large Eddy Simulation (LES) · Synthetic jets · Separation control · Ducted hump

## 1 Introduction

The control of flow separation is a subject of major interest in Aerodynamics, especially in relation to highly-loaded wing segments operating in near-stall conditions.

---

A. Avdis (✉) · S. Lardeau · M. Leschziner  
Department of Aeronautics, Imperial College London, London, UK  
e-mail: alexandros.avdis01@me.com

S. Lardeau  
e-mail: s.lardeau@imperial.ac.uk

M. Leschziner  
e-mail: mike.leschziner@imperial.ac.uk

One promising approach to diminishing or suppressing separation is by means of pulsed jets. Although requiring the input of energy and posing significant engineering challenges in a practical setting, such jets offer the important advantage of flexible, on-demand operation, thus avoiding the added drag of fixed passive devices in design conditions, when separation is not present or in danger of being induced. A particularly attractive type of pulsed jet is the synthetic jet. This is formed by alternating suction and blowing strokes, typically with sinusoidal variation in time, so that no net mass transfer takes place over the period of injection. This is usually achieved with an electrically actuated diaphragm in a cavity lying below the jet orifice. Although the injection involves no net mass transfer, it results in a momentum and vorticity transfer, yielding a far-field behaviour similar to that of a continuous jet. In addition to the on-off operational flexibility offered by this method, the electrical actuation allows easy control over the injection strength and frequency, as appropriate to the conditions to be controlled.

The flow-physical processes by which synthetic jets control separation is multifaceted and complex. At the simplest level, the jet represents an obstacle to the oncoming boundary layer and provokes the formation of streamwise vortices near the wall, which promote mixing in the wall-normal direction, thus inhibiting separation. In addition, the injection produces turbulence by extra straining, thus further enhancing the mixing process. These two effects also arise in passive control, by means of fences and other solid vortex generators, as well as continuous jets injected into the boundary layer. However, the presence of unsteadiness complicated the physics of the interaction considerably. The key issue here is the relationship between the frequency of the injection and instability modes in the separated shear layer. It is generally accepted that two modes are especially pertinent: one associated with the formation of Kelvin-Helmholtz waves and related vortices shortly after separation referred to as the *shear-layer instability* and the other being a *flapping instability* affecting the global behaviour of the shear layer and caused by the interaction of the shear layer with the wall on which it reattaches. Experiments (e.g. Yoshioka et al. [33]) as well as simulations (e.g. Dejoan and Leschziner [5]) confirm, at least for a backward-facing-step flow at relatively low Reynolds number, that the control effectiveness of a synthetic slot jet, injected at the step edge, depends on its frequency and is closely related to the flapping-mode instability of the separated shear layer. In contrast, the role of the shear-layer instability is unclear, and its importance is drawn into question by the fact that unsteady RANS computations return a qualitatively correct response of the time-mean separation region to synthetic-jet actuation (e.g. Dejoan et al. [5]).

Gaining insight into the operational characteristics and/or fundamental interactions of separation control with synthetic jets has been the objective of a substantial number of experimental and computational studies, performed especially over the past decade, thus reflecting an increased awareness of the importance of drag reduction and energy efficiency in the context of civil aviation. In terms of injection geometry, these studies may be divided into two groups, one involving circular jets and the other high-aspect-ratio slot jets. It is the latter group to which the present work pertains. Apart from the fundamentally-oriented studies already noted above, synthetic slot jets have been investigated experimentally by Seifert et al. [25], Amitay et al. [1], Parekh et al. [20], Gilarranz et al. [8], and Greenblatt et al. [9, 10], the

first four in aerofoil geometries and the last two involving injection into a ducted boundary layer separating from a hump. Of these experiments, those by Greenblatt et al. [9, 10] (Fig. 1) have recently become a preferential focal and reference point for several computational studies designed to answer the question as to whether the fundamentals of synthetic-jet injection can be captured with statistical models and simulation methods. Both the experiments and a number of computational solutions were the subject of a workshop recently hosted by the NASA Langley Research Centre [23]. Particular merits of these experiments include the availability of PIV data for mean velocity, phase-averaged velocity and second moments for both the un-actuated (baseline) condition as well as pure suction and mass-less injection.

In contrast to experiments, even if employing time-resolved PIV, the computational prediction of synthetic jets with scale-resolving simulation techniques offers the capability of resolving the broad range of spatial and temporal scales of the entire three-dimensional flow field, and of illuminating the detailed structural features arising from the interaction between the jet and the flow to be controlled. However, such computations face major challenges. First, a serious resolution problem is posed by the geometric scale disparity, arising from the very small size of the jet orifice in comparison with the very large active computational domain. Second, the jet-exit conditions are usually unknown in detail, as these vary rapidly in time in a complex fashion and are also affected by the interaction between the jet-actuation system (including the cavity with its acoustic properties) and the outer flow to be controlled. This complexity and the small size of the orifice prevent an accurate measurement of the jet conditions. Third, the flow approaching the injection location contains an influential boundary layer, the turbulent structure of which is likely to be extremely important. This flow cannot be computed from its inception, however, simply because this would be untenably expensive. Hence, inflow conditions must be generated by means of a separate simulation or a suitable synthetic turbulence-generating method, subject to mean-flow constraints. Fourth, the Reynolds number of the experimental flow is generally too high for a simulation to resolve the near-wall layer in all its details. Hence, an approximate technique, bridging the viscous sublayer, is needed. Finally, the computational domain, whether ducted or not, is large, requiring an extensive numerical grid to achieve adequate resolution. This includes the need to accommodate a large spanwise domain, even if spanwise homogeneity may be assumed to prevail. As will be shown later, the flow is characterised by Streamwise-elongated structures, such that the spanwise extent of the computational domain must be of order 4 times the thickness of the active wall-normal sheared region, that is the separated zone and the free shear layer above it, and the recovering wake region following reattachment.

Of the configurations examined by Greenblatt et al. [9, 10], one particular set of conditions has been the subject of preferential attention. This entailed the injection of a synthetic jet into the separated base flow at a frequency corresponding to a Strouhal number of 0.216, based on the hump height, and at a peak velocity of 0.768 of the free-stream velocity. The attraction to this case is rooted in the observation, made by Yoshioka et al. [33], that the reduction in the size of the recirculation zone behind a backward-facing step reaches a maximum at a similar Strouhal number, as a consequence of the interaction of the pulsed jet with the flapping instability mode. Moreover, the ratio of peak velocity to the outer velocity of the layer approaching

separation is similar in both flows. In such circumstances, the injection results in a material reduction, as opposed to elimination, of the separated region. The correct prediction of this response is regarded as an especially sensitive test of a computational scheme being applied to synthetic-jet-based control.

There have been a number of previous computational studies of the flow under consideration herein. These will be considered as part of the discussion to follow, by reference to a table listing relevant references, the method employed and the principal results obtained. The outcome of some of the studies was presented at the NASA workshop mentioned earlier [23] and others were reported more recently at an ERCOFTAC workshop [31]. A conclusion emerging, especially from the latter workshop, is that RANS methods, which do not account for spanwise variations and structure, are generally unable to represent the flows under consideration with credible realism, partly because the baseline flow is wrongly predicted. As will be shown later, there are also considerable variations among the results of simulations, although the various LES solutions (in contrast to the DES) show a qualitatively correct decline in the recirculation length. Clearly, this is a challenging case, with the solution evidently dependent on the resolution and the manner in which the jet injection and the inflow conditions are prescribed.

This paper reports the outcome of a LES study of the above configuration, both without and with the synthetic jet, the latter at the Strouhal number 0.216. The study distinguishes itself from earlier ones in several respects. First, much attention was paid to the correct representation of the boundary-layer conditions at the inflow boundary. Second, the spanwise extent of the domain is larger than in previous simulations. Third, two options of prescribing the injection conditions were investigated. Finally, Proper Orthogonal Decomposition is used to investigate the dynamics of the flow in the regions of separation, recirculation and reattachment, with particular emphasis placed on the identification of coherent structures. The simulations are shown to yield a markedly better representation of both flow conditions than achieved in most previous studies.

## 2 Flow Configuration

Figure 1 provides a schematic representation of the configuration being examined. Simulations were performed for both the baseline and the jet-controlled case, the former needed to judge the predicted effectiveness of the actuation in the latter. A canonical turbulent boundary layer was allowed to develop upstream of the hump, following a prescription of inflow conditions derived from a precursor simulation, by a process explained later. Table 1 lists the geometric and flow parameters of the computed cases. The principal parameters are: hump chord  $C = 7.78 h$ , where  $h$  is the hump height, hump width (to end plates),  $w = 1.439 C$  and Reynolds number,  $Re_C = 935, 892$ , based on the free-stream velocity  $U_\infty$  and hump chord  $C$ .

In the controlled case, the synthetic jet is located at 65% of chord, close to the time-mean line of separation. The jet was created by oscillating the lower surface of a cavity lying below the jet orifice by means of an *actuator assembly* incorporating acoustic devices. A range of frequencies and jet-momentum coefficients were examined in Greenblatt et al. [10], but only one case is considered herein. The

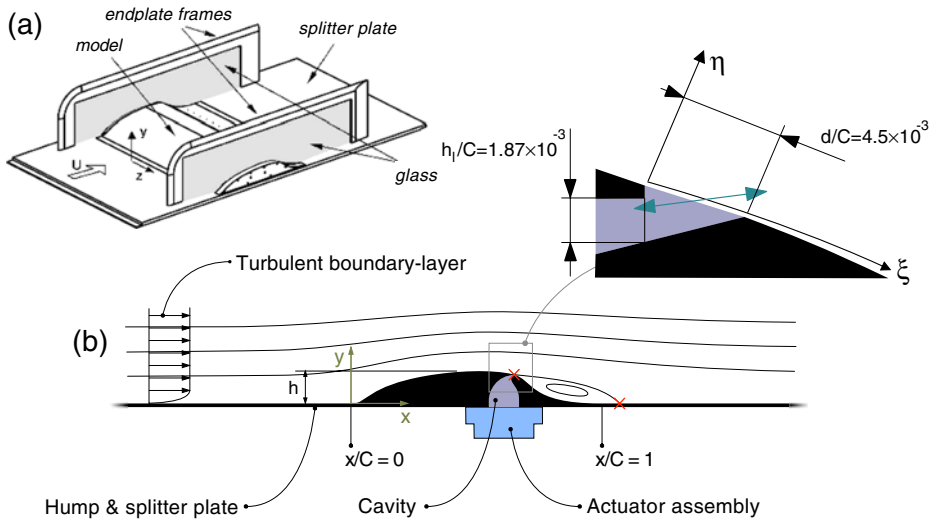


**Fig. 1** The hump configuration being considered. **a** Schematic of the experimental apparatus, taken from Greenblatt et al. [9, 10]; **b** Schematic of the side view

**Table 1** Flow parameters for the hump configuration [9, 10]

Hill geometry & flow parameters			
$C$	Hump chord		$7.78 h$
$h$	Hump height		$0.13 C$
$w$	Model width, between the endplates		$1.44 C = 1.39 h$
$U_\infty$	Free stream velocity		$34.6 \text{ m/s}$
$Re_C$	Chord Reynolds number		$935, 892$
	Mach number		$0.1$
$d$	Synthetic jet orifice width		$4.5 \times 10^{-3} C$
$h_l$	Orifice width in the vertical direction below upstream orifice lip		$1.87 \times 10^{-3} C$
	Orifice location along the streamwise direction, upstream lip		$0.654 C$
Jet operation parameters			
$f_{\text{jet}}$	Jet frequency		$138.5 \text{ Hz}$
$X$	Distance from the slot to the mean reattachment location,		$0.46 C$
$F^+$	Dimensionless jet frequency, based on $X$ and $U_\infty$		$0.77$
$St_{\text{jet}}$	Dimensionless jet frequency, based on $h$ and $U_\infty$		$0.216$
$U_{\text{max}}$	Jet peak velocity		$0.768 U_\infty$
$C_\mu$	Jet momentum coefficient		$0.0011$
Boundary layer quantification at $x/C = -2.14$			
$\delta$	Boundary-layer thickness	Baseline case	$0.07 C = 0.55 h$
		Synthetic-jet case	$0.05 C = 0.43 h$
$\delta^*$	Displacement-thickness	Baseline case	$9.4 \times 10^{-3} C = 0.073 h$
		Synthetic-jet case	$8.5 \times 10^{-3} C = 0.066 h$
$H$	Boundary-layer shape factor	Baseline case	$1.30$
		Synthetic-jet case	$1.34$
$Re_\theta$	Momentum-thickness Reynolds number	Baseline case	$6771$
		Synthetic-jet case	$5904$

injection conditions are defined in terms of the dimensionless frequency  $F^+$  and the momentum coefficient  $C_\mu$ :

$$F^+ = \frac{f_{\text{jet}} X}{U_\infty} \quad (1)$$

$$C_\mu = \frac{2h_l}{C} \frac{\overline{U_{\text{jet}}^2(t)}}{U_\infty^2} \quad (2)$$

where  $X$  is the distance between the mean reattachment location in the baseline case and the jet slot, along the streamwise direction and  $h_l$  is the vertical height of the jet opening, just below the upstream lip of the jet orifice (cf. Table 1 and Fig. 1).  $\overline{U_{\text{jet}}^2(t)}$  is the mean-square of the spatially averaged velocity over the jet orifice. Hot-wire measurements of the peak jet velocity are also documented in Greenblatt et al. [10] (cf. Table 1). Assuming the distribution of velocity to be uniform over the jet orifice and to vary harmonically in time, equation (2) becomes

$$C_\mu = \frac{h_l}{C} \cdot \frac{U_{\text{max}}^2}{U_\infty^2} \quad (3)$$

The most detailed measurements are available for  $F^+ = 0.77$  ( $f_{\text{jet}} = 138.5$  Hz) and  $C_\mu = 0.0011$  [10, 23], and this is the case on which attention focuses herein. Table 1 also lists the jet Strouhal number  $St_{\text{jet}} = (f_{\text{jet}} \cdot h)/U_\infty$ , where  $h$  is the hump height.

The boundary-layer thickness, shape factor and the momentum-thickness Reynolds number, at  $x/C = -2.14$  (with the origin shown in Fig. 1b), are also given in Table 1. These quantities were calculated from velocity measurements obtained with a pitot probe. The boundary-layer parameters for the baseline and synthetic-jet cases are slightly different, as seen from Table 1. These differences arose from blockage effects caused by protrusions from the underside of the laboratory hump, not present in the baseline case, thus leading to a thicker boundary layer in the baseline case.

### 3 Computational Methodology

#### 3.1 Numerical method and grid

Implicitly filtered LES momentum and continuity equations for incompressible flow were solved over a general non-orthogonal, boundary-fitted mesh. The numerical strategy was based on the co-located finite-volume approach. In order to suppress unphysical oscillations, associated with pressure-velocity decoupling, the scheme includes a practice equivalent to that introduced by Rhie and Chow [22]. Within this framework, the fluxes are approximated by central differences, with a minimally diffusive dynamic wigggle-detector used to eliminate odd-even oscillations, and time advancement utilized a fractional-step scheme within which the time derivative was approximated by a third-order Gear scheme (Fishpool et al. [6]). In this two-step process, the provisional velocity field resulting from advancing the solution with the flux operators is corrected by a pressure gradient which is evaluated by projecting the provisional solution onto a divergence-free velocity field. To this end, the pressure is computed as a solution to the pressure-Poisson problem using a multigrid scheme.

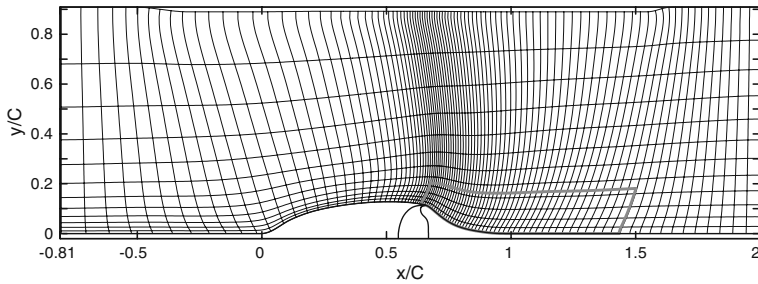


**Fig. 2** Grid used for the present computations. For clarity, only every eighth grid line is shown. The framed area downstream of the jet orifice was used for sampling data for the POD analysis (see Section 4.4)

The subgrid-scale stresses were approximated by the dynamic Smagorinsky model of Germano et al. [7] and Lilly [14].

The grid used for the computations reported below comprises  $768 \times 96 \times 128$  cells in the streamwise ( $x$ ), cross-stream ( $y$ ) and spanwise ( $z$ ) directions, respectively. The spanwise grid covers a slab, assumed to be periodic, of depth  $0.4 C$ , i.e. 3.12 times the hump height. The principal features of the grid in any spanwise plane are conveyed by Fig. 2, in which only every eighth grid line is shown. The computational domain extends from  $x/C = -0.81$  to  $x/C = 2$  in the streamwise direction. In the cross-stream direction,  $y/C = 0$  corresponds to the splitter-plate surface containing the hump, and the grid extends to  $y/C = 0.909$ , corresponding to the wall of the wind tunnel in the experiment. As regards the shape of the upper wall, it is noted in Fig. 2 that this wall features a slight constriction from  $x/C \approx -0.52$  to  $x/C \approx 1.64$ . This is done to mimic the blockage effect of the end plates in the experimental configuration, shown in Fig. 1a (see Gatski and Rumsey [23] for details).

### 3.2 Boundary conditions

The velocity at the inflow of the computational domain was obtained from a separate quasi-streamwise-periodic *precursor simulation* of a turbulent boundary-layer in zero pressure gradient, with rescaling effected to account for the boundary-layer development (Lund et al. [15]). The extent of the precursor and the main simulations is shown in Fig. 3. As stated in Table 1, the experimental momentum-thickness Reynolds number at  $x/C = -2.14$  was  $Re_\theta = 6771$  for the baseline case and  $Re_\theta = 5904$  for the synthetic-jet case. These values were used to specify the mean-velocity profile, so as to comply with the log-law and have the requisite momentum-thickness Reynolds numbers. Turbulent fluctuations were then extracted during the simulation from a downstream plane and super-imposed onto the mean-flow profile. Instantaneous fields were collected over 10,000 time-steps (corresponding to 4.47 flow-through times of the precursor simulation or 4.1 flow-through times of the main simulation) at the plane  $x/C = -0.81$ . These were then fed explicitly into the main simulation. Given the differences in the boundary layer at  $x/C = -2.14$  noted in Table 1 and Section 2, separate precursor simulations were performed for the baseline and the synthetic jet cases. Figure 4 compares the time-mean streamwise velocity profiles and Reynolds-stress profiles, derived from the 10,000 realisations

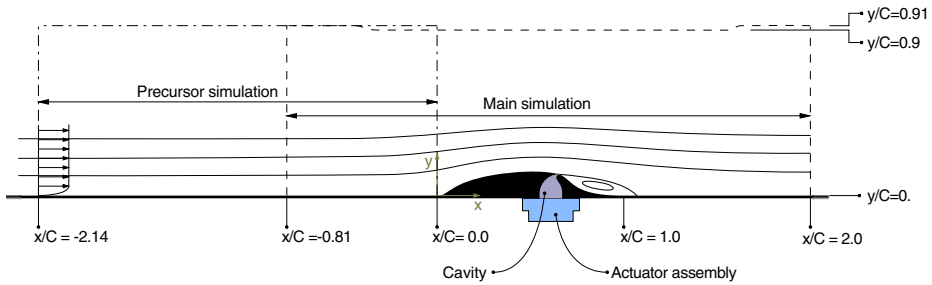


**Fig. 3** Schematic of the hump configuration, including the domains used in the main simulation and the simulation generating inflow conditions

collected at the plane  $x/C = -0.81$ . As seen, the differences between the two sets of profiles at  $x/C = -0.81$  are insignificant. Hence, the quantification of the control effectiveness of the jet injection may be claimed to be virtually unaffected by the small differences in the inlet conditions.

At the outflow plane of both the main and the precursor simulations, a convective outflow boundary condition was used, following Pauley et al. [21], wherein the velocity vector at the outflow boundary was obtained by solving a pure convection equation with the convection velocity kept constant at its free-stream value.

The high Reynolds number of the flow precluded a full resolution of the near-wall layers. Figure 5 shows the distribution of cell dimensions, normalised by  $\nu/u_\tau$ , in the layer of cells closest to the lower wall. The friction velocity,  $u_\tau$ , used for scaling the cell dimensions has the fixed value prevailing at the domain inlet. While the

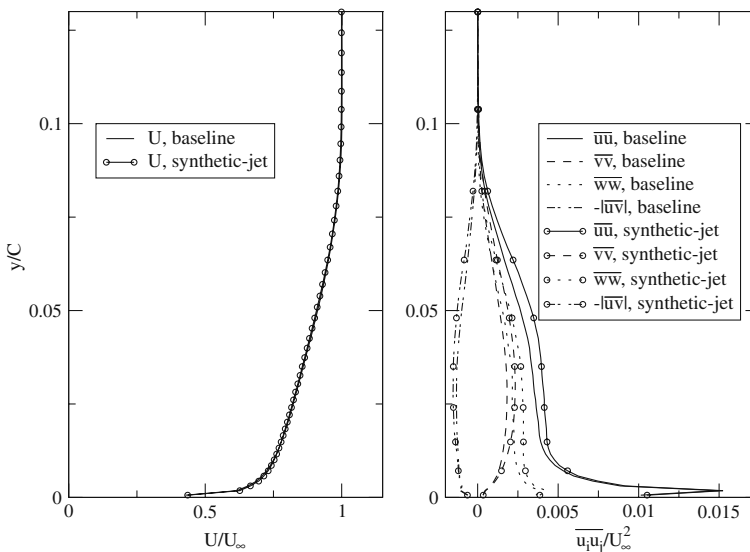


**Fig. 4** Streamwise velocity (left) and Reynolds stresses (right) calculated from the stored realisations during the precursor simulations at  $x/C = -0.81$



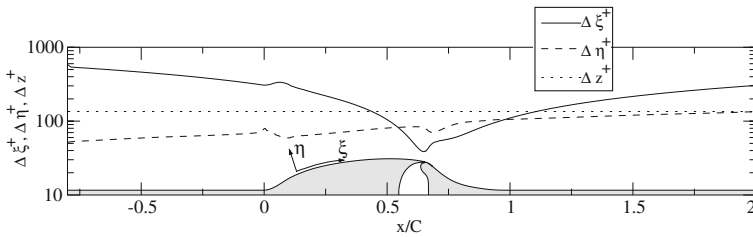


**Fig. 5** Distributions of cell dimensions in viscous units adjacent to the hump surface

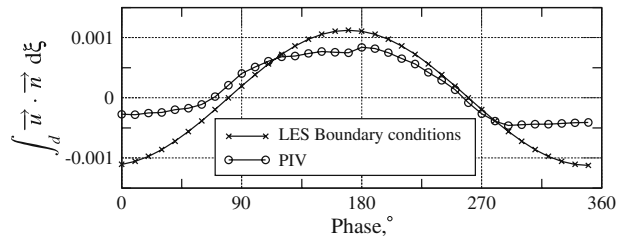
streamwise-local value could have been used, in principle, this varies little until the separation point is approached, as will be shown later by reference to distributions of the skin-friction coefficient. However, beyond this region, use of the local value is clearly inappropriate for scaling the distance, because the flow is separated. As suggested by Fig. 5, the centroids closest to the wall were at a distance  $10 \leq \eta^+ \leq 20$ . To bridge near-wall layer, the *two-layer wall law* of Deardorff [4] was used in precursor simulations, while the *Werner-Wengle wall law* (Werner and Wengle [32]) was used in the main simulations. This approach might seem overly simple in the light of recent developments in the area of LES-RANS hybrids. However, in the present case, the separation location, whilst not fixed, is constrained to occur within a narrow streamwise strip due to the high-curvature of the hump surface at 65% of the chord. In such circumstances, the flow is less sensitive to the precise details of the processes very close to the wall than in situations in which separation occurs over a gently curved surface, such as a stalling aerofoil. The application of an elaborate, and considerably more costly, LES-RANS hybrid (e.g. Tessicini et al. [30]) was deemed unnecessary.

The cavity below the jet orifice was not resolved. To do so would have resulted in a major increase in computational resource, especially as acoustic features of the cavity would have had to be accommodated in the simulation. Instead, the conditions at the orifice were extracted from the experiments. In a first attempt, the velocity distribution (in terms of both magnitude and direction) at the orifice was derived by interpolating the PIV data in the vicinity of the jet orifice. As shown in Fig. 6, the phase-varying volume flow rate through the jet orifice does not integrate to zero, the error being as large as 30% of the r.m.s. value. In simulations in which the velocity profiles thus extracted were used as boundary conditions, the control effect of the jet on the separation-bubble length was observed to be negligible. This practice was therefore deemed unrealistic. Instead, and following You et al. [35], the jet-orifice conditions were analytically generated, so as to match the peak volume flux and the momentum coefficient calculated from hot-wire measurements (Greenblatt et al. [10]). In specific terms, the streamwise component of the velocity vector over the jet orifice was approximated by a parabolic profile varying sinusoidally in time, while the cross-stream component was set to zero, i.e.:

$$u_{\text{jet}}(\xi, t) = 6U_{\text{max}} \left[ \frac{\xi}{d} - \left( \frac{\xi}{d} \right)^2 \right] \cos \left( 2\pi \cdot f_{\text{jet}} \cdot t - \frac{\pi}{36} \right)$$

$$v_{\text{jet}}(\xi, t) = 0 \quad (4)$$

**Fig. 6** Volume flow rate per unit spanwise length derived from profiles extracted from the PIV measurements, relative to that obtained from the profile in equation (4)



where  $\xi$  and  $d$  are defined in Fig. 1b. The phase-variation of the volume flow rate through the jet orifice resulting from equations (4) is included in Fig. 6.

## 4 Results and Discussion

### 4.1 Instantaneous view

Instantaneous snapshots of the flow, both without and with the synthetic jet active, are given in Fig. 7. The fields are displayed through iso-surfaces of the second invariant of the velocity-gradient tensor—the  $Q$  criterion,  $Q = \frac{1}{2} (\Omega_{ij}\Omega_{ij} - S_{ij}S_{ij})$ , where  $\Omega_{ij}$  is the vorticity tensor and  $S_{ij}$  is the rate-of-strain tensor,  $S_{ij} = \frac{1}{2} \cdot \left( \frac{\partial u_i}{\partial x_j} + \frac{\partial u_j}{\partial x_i} \right)$ . The iso-surfaces are coloured (shaded) with contours of the streamwise velocity.

The flow is seen to separate, with and without the jet, over the aft part of the jet, and it recirculates downstream of the hump. In the baseline case, the  $Q$  iso-surfaces do not reveal the presence of large-scale structures in the separated shear-layer. This is not entirely surprising, for the  $Q$  criterion is known to bring out, preferentially, small-scale features, which are characterised by steep velocity gradients. However, spectra presented in this subsection and POD analysis in Section 4.4, suggest that there are large-scale structures also present in the baseline flow. When the synthetic jet is introduced, this is observed to provoke major periodic fluctuations in the flow, which are brought to light by the  $Q$  iso-surfaces as large-scale vortices, aligned with the spanwise direction, upon which the fine-scale structure is super-imposed. Large spanwise vortices, also brought out more clearly later by way of phase-averaged fields, are typical features in separated flows that are perturbed in a manner similar

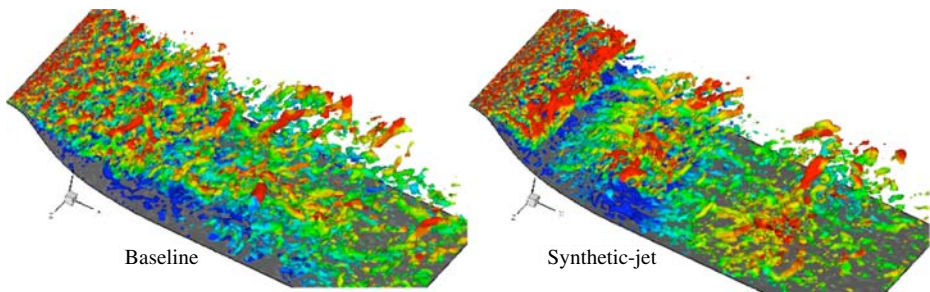


**Fig. 7** Iso-surfaces of the  $Q$ -criterion, from instantaneous results for the baseline flow (left-hand side) and the jet-actuated flow (right-hand side)

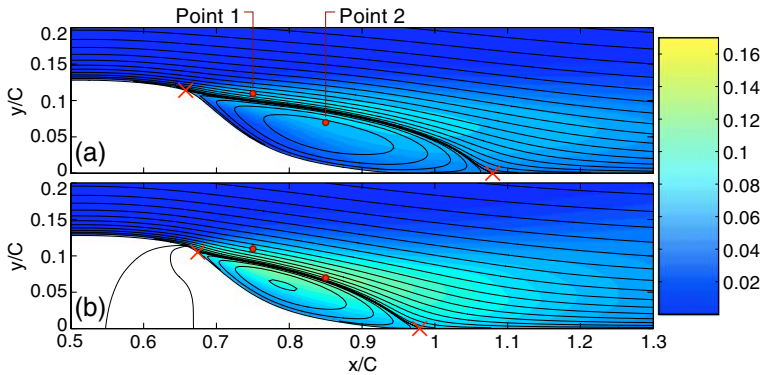


**Fig. 8** Time-averaged streamlines superimposed on contours of time-averaged turbulence kinetic energy **a** baseline case **b** jet case. The points where time-series of the velocity were sampled are also shown

to the present case when the perturbation frequency is in the range  $F^+ = O(1)$ , and these have been documented in experimental studies by Nishri et al. [18], Yoshioka et al. [33] and Gilarranz et al. [8], as well as numerical simulations by Parekh et al. [20], Dejoan and Leschziner [5], You and Moin [34] and Dandois et al. [3]. The intensity of these features reflects the responsiveness of the flow to the jet-actuation parameters imposed, in particular the frequency. It has been pointed out already that the choice of Strouhal number,  $St_{jet} = 0.216$ , is linked to the observation that this value is close to the flapping instability of the shear layer. To investigate this, time-series have been collected at the two points shown in Fig. 8: in the initial part of the shear layer, close to the separation point (Point 1), and further downstream, in the middle of the separated region (Point 2). From these series, energy spectra have been derived.

Figure 9 shows pre-multiplied spectra as a function of the Strouhal number,  $(f \cdot h) / U_\infty$ . For the baseline case, there is a clear shift of the peak from a Strouhal

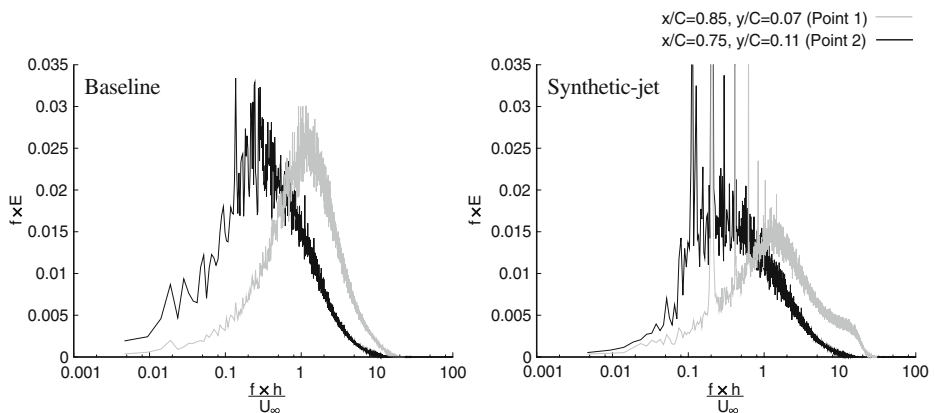


**Fig. 9** Pre-multiplied spectra for the Baseline case (left) and the injection case (right) for two different positions in the separated shear layer

number of around 1, at point 1, to a value of about 0.2 in the middle of the shear layer, thus close to the frequency of the jet. With the jet switched on, the spectrum then exhibits extremely high peaks at point 2, around the Strouhal number 0.2, these peaks rising far above the limiting value of 0.035 on the ordinate of Fig. 9. Hence, the spectra provide evidence of a preferential receptivity of the shear layer to the periodicity of the jet and also imply the presence of associated structures, which are too weak to be visible in the instantaneous view in Fig. 7.

#### 4.2 Mean-flow field

An overall view of the predicted time-averaged flows, and thus a global impression of the control effectiveness of the synthetic-jet actuation, is provided in Fig. 8 by way of stream-function contours superimposed on shaded contours of turbulence energy. These plots, as well as other statistical data presented later, have been obtained by integration over 300,000 time steps, corresponding to 14.8 flow-through times, in the baseline case and 13.6 flow-through times (or 64.4 jet-injection periods) in the actuated case. The crosses in Fig. 8 indicate the locations of zero shear stress at the wall, signifying corresponding separation and reattachment points. As seen, the actuation is predicted to bring about a 30% reduction in the size of the recirculation zone. This compares well with the experimentally observed reduction by 28%. For the baseline case, the predicted mean separation and reattachment locations are  $x_s/C = 0.658$  and  $x_r/C = 1.079$ , respectively, against the corresponding experimental values of  $x_s/C = 0.665 \pm 0.005$  and  $x_r/C = 1.10 \pm 0.005$ . When the jet is introduced, the simulations predict  $x_s/C = 0.674$  and  $x_r/C = 0.979$ , compared to the corresponding experimental values of  $x_s/C = 0.676$  and  $x_r/C = 0.990$ . As is shown in Table 2, this agreement is far better than that achieved with RANS computations and most previous simulations. As would be expected, and confirmed by Fig. 8, the jet injection brings about a marked increase in total “turbulence” energy around the separated shear layer, consistent with the increased level of momentum mixing that manifests itself in a shorter recirculation zone. This elevation of energy reflects, on the one hand, the increased turbulence activity provoked by additional, jet-induced straining and, on the other, the additional fluctuation energy associated with the periodic flapping.

Table 2, already referred to above, lists most of the published computational studies directed towards the configuration shown in Fig. 1. For each study, the numbers of cells in the streamwise, wall-normal and spanwise directions are given, along with the domain size and numerical strategy (LES, DES, RANS). The present study is also listed for comparison. The separation and reattachment locations are noted, but in some publications the separation location is not reported by the respective investigators, in which case the value given is the location of the jet orifice. Also listed are the size of the separation bubble, normalised with the hump chord, and the difference from the experimental value in the baseline case. Thus, the rightmost column in Table 2 lists the % error in the bubble length for the baseline case and the % change in the bubble length relative to the baseline case, when the jet is introduced:

$$\Delta, \Delta_r = \frac{(x_{r,\text{exp}} - x_{s,\text{exp}}) - (x_{r,\text{comp}} - x_{s,\text{comp}})}{x_{r,\text{exp}} - x_{s,\text{exp}}} \cdot 100 \quad (5)$$

**Table 2** Principal parameters and results of past computational studies of the present flows

Authors (type)	Grid	Domain size		Separation & reattachment		Bubble length	$\Delta(\%)$	
		$\frac{L_x}{C}$	$\frac{L_z}{C}$	$\frac{L_z}{h}$	$\frac{x_s}{C}$	$\frac{x_r}{C}$		$\frac{x_r - x_s}{C}$
Baseline case								
Ref. [9] (Exp)					0.665	1.10	0.435	
Current (LES)	$768 \times 96 \times 128$	2.81	0.4	3.12	0.658	1.079	0.421	-3
Ref. [35] (LES)	$721 \times 161 \times 65$	4.5	0.2	1.56	$\approx 0.65$	1.09	0.44	1
Ref. [24] (LES)	$426 \times 145 \times 64$	6.14	0.152	1.18	0.667	1.114	0.447	3
Ref. [17] (ILES)*	$818 \times 151 \times 165$	5.2	0.2	1.56	$\approx 0.65$	1.139	0.498	12
Ref. [24] (DES)	$426 \times 145 \times 28$	6.14	0.2	1.56	0.663	1.121	0.458	5
Ref. [12] (DES)	$841 \times 101 \times 41$	12.74	0.121	0.94	$\approx 0.65$	1.13	0.48	10
Ref. [12] (3D RANS)	$4.9 \times 10^6$	12.74	With endplate		$\approx 0.65$	1.24	0.59	36
Ref. [24] (2D RANS)	$426 \times 145$	6.14	-	-	0.670	1.125	0.455	5
Ref. [12] (2D RANS)	$841 \times 217$	12.74	-	-	$\approx 0.65$	1.28	0.63	45
Synthetic-jet case								
Ref. [10] (Exp)					0.676	0.990	0.314	$\Delta_r(\%)$ -28
Current (LES)	$768 \times 96 \times 128$	2.81	0.4	3.12	0.674	0.979	0.305	-30
Ref. [35] (LES)	$721 \times 161 \times 65$	4.5	0.2	1.56	$\approx 0.65$	1.01	0.36	-17
Ref. [24] (LES)	$426 \times 145 \times 64$	6.14	0.152	1.18	0.671	1.050	0.379	-13
Ref. [17]-LA (ILES)*	$818 \times 151 \times 165$	5.2	0.2	1.56	$\approx 0.65$	1.097	0.447	2
Ref. [17]-HA (ILES)*	$818 \times 151 \times 165$	5.2	0.2	1.56	$\approx 0.65$	0.997	0.347	-20
Ref. [24] (DES)	$426 \times 145 \times 28$	6.14	0.2	1.56	0.662	1.110	0.448	3

The experimental results and the results of the present study are also listed for comparison. Studies marked with an asterisk were performed at a lower Reynolds number than that of the experiment. “LA” identifies the lower injection amplitude, which is the one pertinent of the present study. “HA” identifies a higher injection amplitude

where  $x_{r,\text{exp}}$  and  $x_{s,\text{exp}}$  denote the mean reattachment and separation locations in the experiment of the baseline case.  $x_{r,\text{comp}}$  and  $x_{s,\text{comp}}$  denote the mean reattachment and separation location obtained from the simulation results.

As regards the LES of Šarić et al. [24], it is relevant to point out that spanwise two-point correlations of the velocity components have provided clear indications that their spanwise domain  $L_z/h = 1.18$  was insufficient for capturing the largest scales in the flow. The spanwise domain of You et al. [35] is only marginally larger, and these authors report a significant sensitivity of the results to the spanwise box size. Compared with these two studies, the present simulations were performed over a substantially larger computational domain in the spanwise direction and with higher streamwise resolution. On the other hand, the cross-stream resolution is slightly lower. The DES by Krishnan et al. [12] of the baseline flow was also performed over a small spanwise slab, and this may be one contributor to the 10% difference between the computed and measured recirculation lengths, as is implied by the closer agreement achieved by Šarić et al. [24] with their DES over a larger (but still too small) spanwise slab. A relatively small spanwise slab was also used in the LES by Morgan et al. [17] for the present injection condition,  $(C_\mu, F^+) = (0.0011, 0.77)$ , as well as a much higher forcing amplitude,  $(C_\mu, F^+) = (0.0075, 0.77)$  (qualified as “LA” and “HA” in Table 2). Although their study was performed with exceptionally high resolution, the simulated Reynolds number,  $(Re_C = 2.0 \times 10^5)$ , was substantially lower than the experimental value, so that the agreement with the data of Greenblatt et al. [9, 10], while close, is not quantitatively safe.

In the three-dimensional RANS solutions of the baseline case reported by Krishnan et al. [12], the computed geometry included the end-plate (shown in Fig. 1a), while symmetry conditions were prescribed on the geometry’s centre plane. This computation gave a seriously excessive length for the separation region. In contrast, an equivalent two-dimensional RANS computation gave a result far closer to the experiment, but this result must be assumed to be fortuitous. An interesting message derived from a comparison of these two calculations was that blockage in the wind-tunnel section caused by the end-plates had a not insignificant effect on the pressure coefficient along the surface of the hump. Consistently, the two-dimensional RANS solution of Krishnan et al. [12] and Šarić et al. [24], as well as the DES solution of Krishnan et al. [12], resulted in an excessive pressure coefficient along the hump surface, upstream of the separation location. It is this observation that led to the introduction of the slight constriction of the geometry by an artificial reshaping of the upper wall (see Figs. 2 and 3). As implied by the distribution of the pressure-coefficient,  $C_p = (1/2) \cdot P / (\rho U_\infty^2)$ , for the baseline case in Fig. 10, the adjustment of the upper wall emulates reasonably well the blockage presented to the flow by the end plates. For the baseline flow, the predicted pressure coefficient agrees well with the experimental variation also downstream of the separation location, indicating that the lateral (wall-normal) shape of the separation bubble has been correctly captured. Agreement for the actuated case is less good, however. The simulation returns a much reduced pressure plateau relative to that of the baseline case, signifying a monotonic pressure recovery, which is consistent with the substantial reduction in the size of the recirculation zone and a downward sloping of the separation streamline, as seen in Fig. 8. In contrast, the measurements appear to suggest, oddly, that the injection results in an initial thickening of the recirculation bubble after separation, and hence acceleration of the flow above the bubble, followed by a rapid reduction

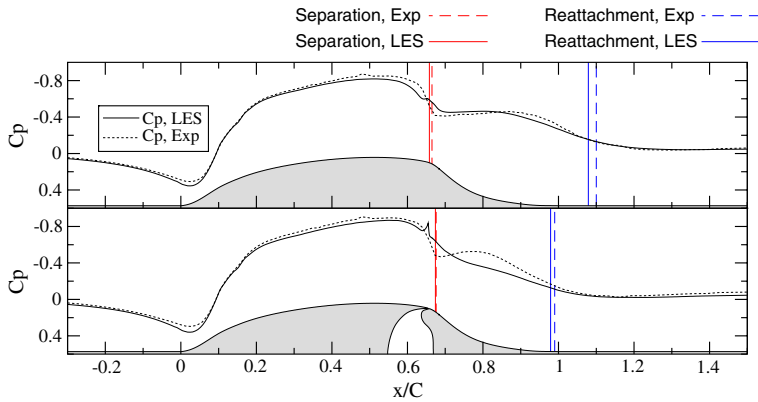
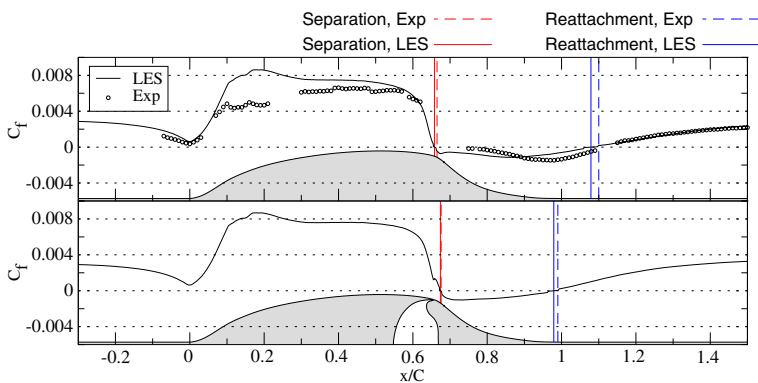


**Fig. 10** Time-averaged pressure coefficient for baseline and synthetic-jet cases

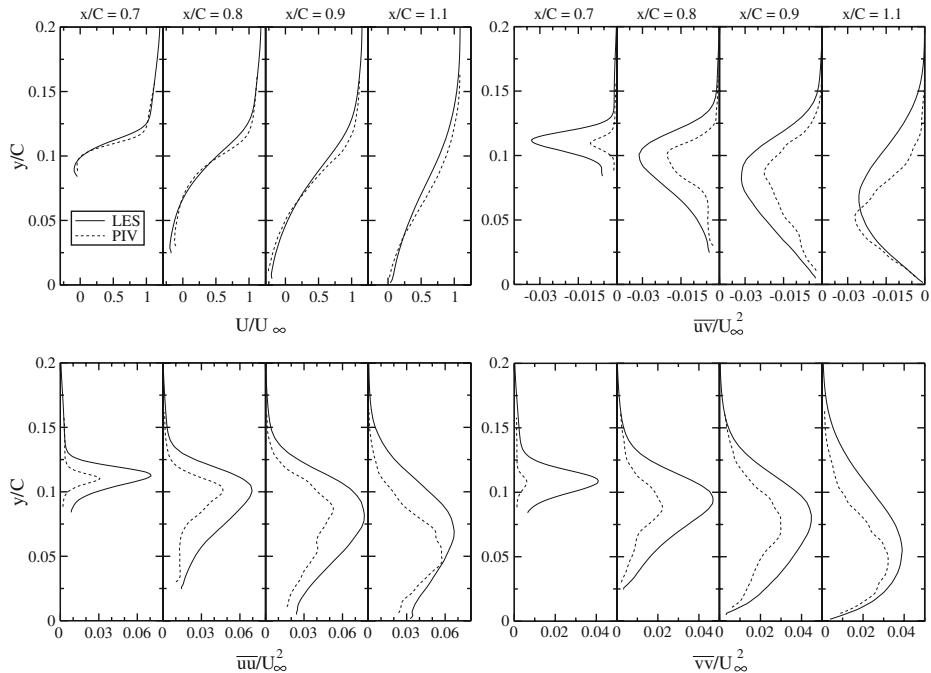
in the thickness and hence rapid pressure recovery beyond the peak thickness at  $x/C = 0.8$ .

Figure 11 presents computed results for the skin-friction coefficient. For the baseline case, experimental data are available, and these are included in the upper plot for comparison. The results, both experimental and computational, need to be viewed with caution: the skin friction is notoriously difficult to measure accurately, while the computational results had to be extracted from the wall function used (*cf.* Section 3.2). Notwithstanding these uncertainties, the results serve to support two arguments. First, they confirm the earlier made statement that use of the streamwise-local friction velocity in Fig. 5 would not change its message significantly upstream of the separation region. Second, they give an encouraging indication that the wall function provides a broadly correct wall boundary conditions for the LES solution, justifying its use in the face of the major resolution challenges posed by this case.

For the baseline case, Fig. 12 compares predicted and experimental profiles of the streamwise velocity, normal stress components  $\overline{uu}$  and  $\overline{vv}$  and the shear stress  $\overline{uv}$  at four streamwise locations. The predicted streamwise velocity profiles are in good



**Fig. 11** Time-averaged skin-friction coefficient for baseline and synthetic-jet cases



**Fig. 12** Profiles of time-averaged streamwise velocity and Reynolds stresses for the baseline case

agreement with the experimental results. However, the thickness of the shear layer is larger than that measured. This is especially visible on the upper part of the shear layer in which the predicted velocity is too low. As might be expected, the predicted stresses also exceed the measured levels, indicating excessive turbulence activity and thus a more extensive spread on the boundary. Yet, the size of the recirculation zone is correct, suggesting that the predictive errors ought not to be large, especially not in the lower edge of the shear layer. Close to the separation location, the differences between computations and corresponding measurements are especially large, but it must be borne in mind here that even very slight differences in the separation location will cause substantial differences in the stresses, as these evolve very rapidly following separation. Nevertheless, the excess in the predicted level occurs over the entire separated region, and is also consistent with the slightly too early reattachment and the excessive width of the separated shear layer—a behaviour opposite to that generally observed in RANS computations, in which the predicted shear stress is often far too low, hence giving rise to an excessively long recirculation region.

Figure 13 shows profiles of the streamwise velocity, normal-stress components  $\overline{u'u'}$  and  $\overline{v'v'}$  and shear stress  $\overline{u'v'}$  for the actuated case, at the same streamwise locations as in Fig. 12. As with the baseline flow, agreement is generally good in respect of the streamwise velocity profiles, and this is consistent with earlier observations on the correctly predicted reduction in the length of the separation bubble. Particular attention is drawn here to the location  $x/C = 1.1$ , for which a comparison of the profiles in Figs. 12 and 13 close to the wall illustrates well the predictive quality achieved. Notwithstanding this success, the profiles provide, here again, evidence of



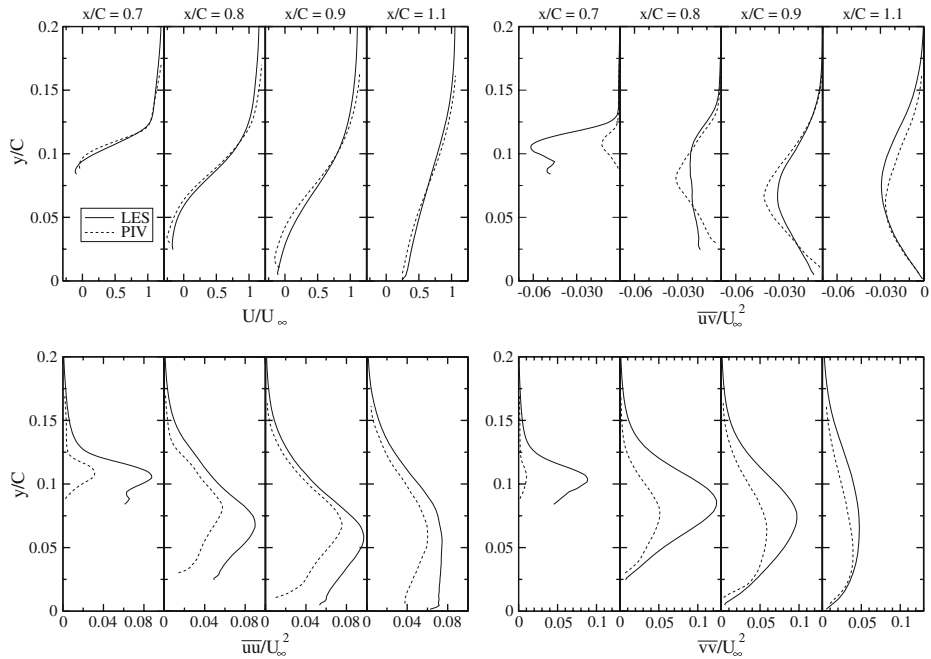


**Fig. 13** Profiles of time-averaged streamwise velocity and Reynolds stresses for the synthetic-jet case

excessive spread in the separated shear layer. Consistently, the computations also predict excessively high normal stresses. Oddly, however, the shear stress appears to be too low beyond  $x/C = 0.8$ . As might be expected, the experiments suggest that the actuation results in an elevation of the shear stress relative to the baseline case, consistent with enhanced mixing. In contrast, the simulation returns shear-stress peaks which are little changed relative to the baseline case. However, the shear stress is high over a lateral extent (across the shear layer) larger than that of the baseline case, and this applies especially to lower parts of the shear layer, consistent with the much lower position of the shear layer when the jet is active (see Fig. 8). A comparison of corresponding normal-stress profiles reveals that the actuation results in a doubling of the transverse stress  $\overline{vv}$  in the middle of the separated shear layer, while the streamwise stress is only modestly elevated. This disproportionate rise in  $\overline{vv}$  is a clear reflection of the flapping of the shear layer, but it appears that the statistical correlation between lateral and streamwise fluctuations is not increased commensurately. A factor likely to contribute to the mismatch in the shear stress at  $x/C = 0.8$  and beyond is the behaviour further upstream. As in the baseline case, the predicted shear stress is extremely high in the initial part of the separated shear layer, and this leads to faster spreading in the early stages of the evolution of the shear layer, thus resulting in a lower shear strain further downstream.

#### 4.3 Phase-averaged statistics

The process by which the separation zone is reduced by the jet injection is illustrated in Fig. 14, which shows phase-averaged contours of streamfunction and turbulence

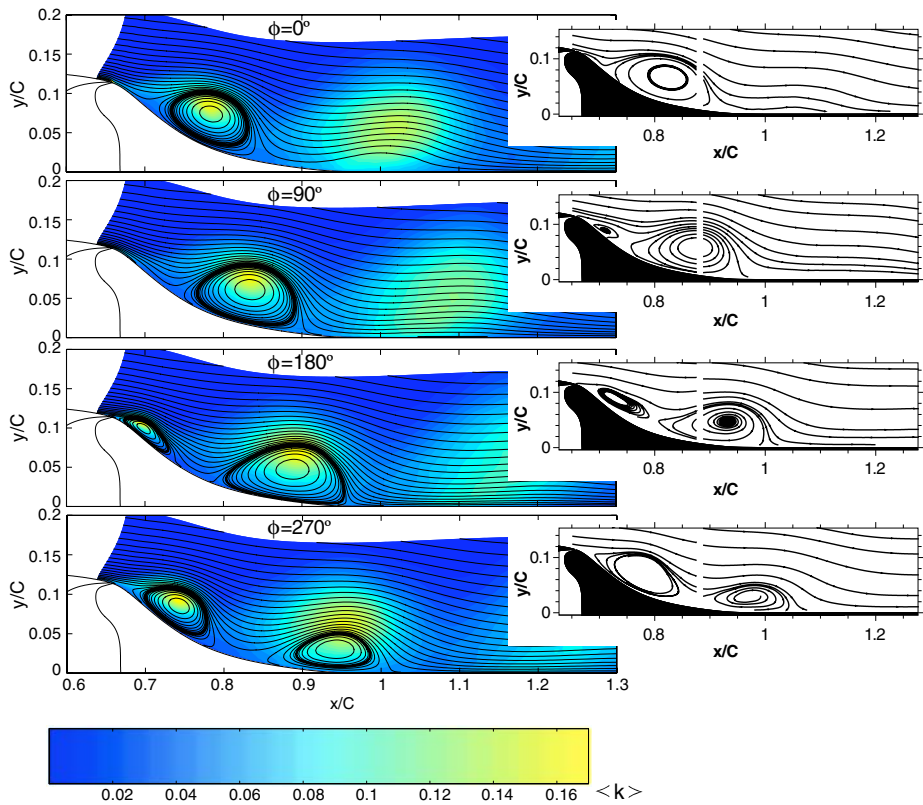


**Fig. 14** Phase-averaged stream-function contours superimposed onto contours of phase-averaged turbulence energy. The smaller inserts show streaklines from the experimental results. Phase  $\phi = 0^\circ$  is close to the time of maximum blowing through the jet orifice, while phase  $\phi = 180^\circ$  is near maximum suction (*cf.* Fig. 6)

energy at four phases of the jet-injection period. Streaklines determined from the corresponding phase-averaged experimental results are also included. It is recalled that phase-averaging was performed over 64 injection periods. It is also noted that phase-averaging relies on the assumption that the injection is effected at a single frequency. While this is so in the simulation, by virtue of the prescription of the injection at the orifice, there is some uncertainty in the experimental data that arises from the fact that the cavity may have introduced sub-harmonics to the basic oscillation of the acoustic devices provoking pressure fluctuations in the cavity.

Both sets of results bring to light the formation of large spanwise vortical structures that evolve along the flow in harmony with the injection periodicity. There is good correspondence between the simulation and the experiment, but it is rather unclear from the latter how the flow behaves between successive rollers. As is seen from the simulation, rollers are separated by significant stretches of attached flow. These progress along the flow at a speed of about 40% of the average flow velocity upstream of the injection location, and this is very close to the speed observed by Dejoan and

Leschziner [5] in their back-step configuration. The vigorous disturbances associated with the large roller-like structures are ultimately responsible for the reduction in the time-averaged separation region through earlier reattachment. As seen from Fig. 14, the highest levels of phase-averaged turbulence energy occur above the spanwise vortices. In contrast, Dejoan and Leschziner [5] and Dandois et al. [3] have observed regions of elevated turbulence energy to occur predominantly *between* successive vortices, rather than above them, and these locations are reported to approximately coincide with positions of elevated phase-averaged strain rate between more closely spaced spanwise vortices.

Figure 15 shows profiles of phase-averaged streamwise velocity at phases  $\phi = 0^\circ$  and  $\phi = 180^\circ$ . Agreement is again generally good, especially when the challenge of correctly predicting (and measuring) phase-averaged second moments are considered. Specifically, as noted earlier, phase-averaging is sensitive to the periodicity of the injection process. The shear-stress profiles at the phase  $\phi = 180^\circ$  deserve particular attention. The normalised shear-stress peak is seen to rise from  $-0.03$  at  $x/C = 0.8$  to  $-0.08$  at  $x/C = 0.9$ , both at the lateral location  $y/C = 0.75$ . Figure 14 shows the former location to lie between rollers, while the latter is above a roller, thus confirming the earlier observation that a marked increase in actuation-induced turbulence activity arises above rollers, where additional shear strain is imparted to the already highly turbulent separated shear layer. A similar causal relationship can also be identified for  $\phi = 0^\circ$ , except that the shear stress drops between  $x/C = 0.8$  and  $0.9$ .

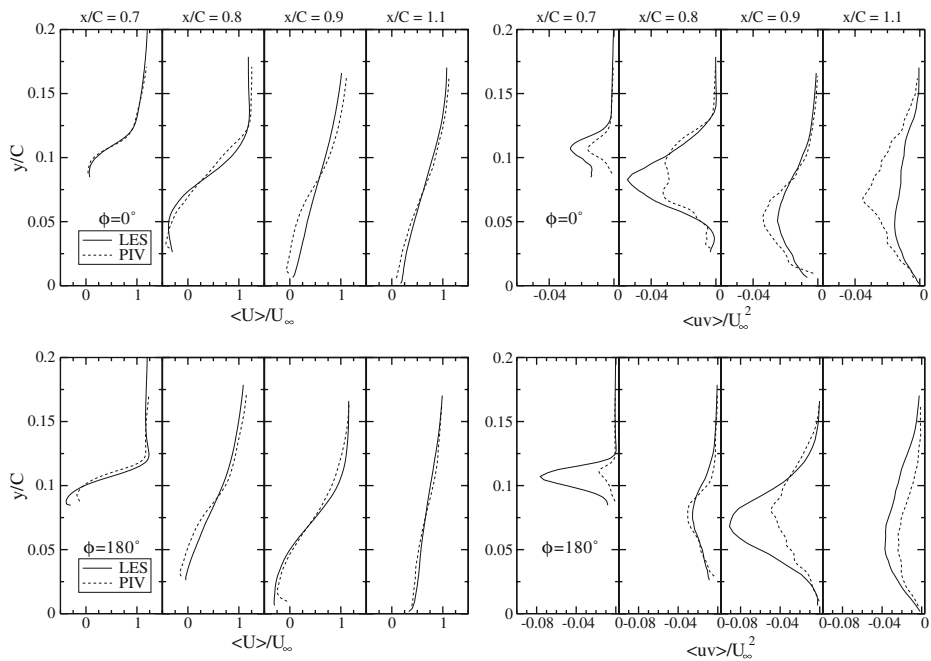


**Fig. 15** Profiles of phase-averaged streamwise velocity and shear stress at  $\phi = 0^\circ$  (top) and  $\phi = 180^\circ$  (bottom)

#### 4.4 Dynamics of the separation region using POD analysis

Among several approaches to analysing structural features of turbulent flows, *Proper Orthogonal Decomposition* offers particular advantages pertinent to the present study. The objective of including POD is to try to identify the relevance and contribution of different modes to the behaviour observed with and without the jet. As regards general aspects of POD, the reader is referred to Holmes et al. [11]. An important fact in the present context is that the *snapshot* variant has been applied herein, using 2 200 three-dimensional snapshots, taken over 28 time units (or in the case of synthetic-jet, 48 jet periods). Due to the large storage requirements associated with the POD analysis, realisations of the flow-field were collected only in the area of separation, recirculation and reattachment. The area in which samples were collected is indicated by the grey lines in Fig. 16 and in Fig. 2. In essence, the velocity field is decomposed into a sum of modes, each multiplied with a corresponding time-dependent coefficient:

$$u_i(\mathbf{x}, t) = \sum_{n=1}^{\infty} \alpha_i^n(t) \cdot \Phi_i^n(\mathbf{x}) \quad (6)$$

where  $u_i(\mathbf{x}, t)$  denotes the velocity component  $i$ ,  $\alpha_i^n(t)$  are the time-dependent coefficients and  $\Phi_i^n(\mathbf{x})$  are the eigenvectors. Since the flow is unbounded (nominally, infinite) in the spanwise direction, the empirical eigenfunctions can be regarded as *plane waves* (Sirovich [26]), and take the form:

$$\Phi_i^n(x, y, z) = \xi_i^q(x, y, k) \exp(-ikz) \quad (7)$$

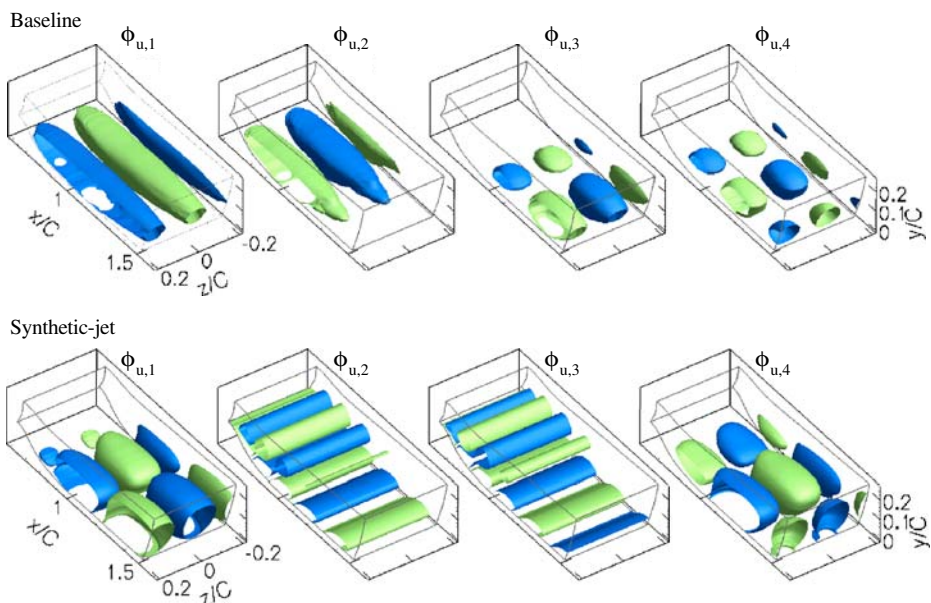


**Fig. 16** Iso-surfaces of the four most energetic POD modes of the streamwise velocity component of the baseline case (*above*) and the synthetic-jet case (*below*). Surfaces are drawn at levels  $\Phi_{u,n} = -0.04$  (blue/dark grey) and  $\Phi_{u,n} = 0.04$  (green/light grey)

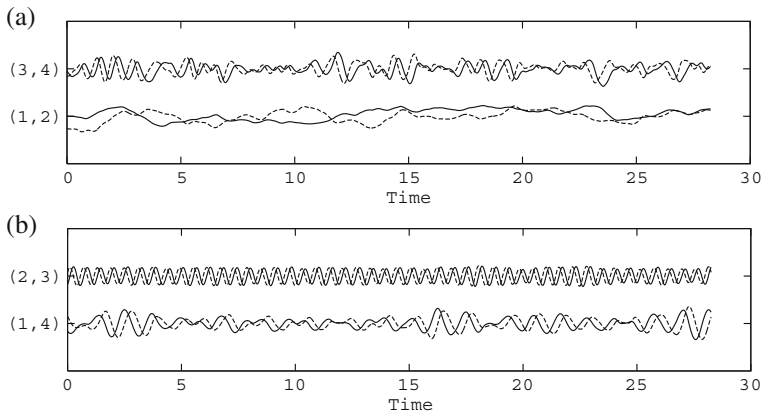


**Fig. 17** Time-dependent coefficients of the four most energetic POD modes of the streamwise velocity component for the baseline case (*above*) and synthetic-jet case (*below*)

with

$$k = 2\pi m/L_z \quad (8)$$

where  $q$  is the so-called quantum number and  $m$  is the number of full waves in the homogeneous ( $z$ ) direction.

Figure 16 shows iso-surfaces of the first four, most energetic, POD eigenvectors for the streamwise-velocity component for both cases. The associated time-coefficients for the same four modes are given in Fig. 17. The corresponding eigenvalues, spatially integrated energy associated with each mode, quantum number  $q$  and  $m$  are given in Table 3.

A comparison of the fraction of spatially integrated turbulence energy associated with the modes for the baseline and synthetic-jet cases (columns 4 and 8 in Table 3) shows the synthetic jet to provoke an increase in energy in the first few modes. The implication is thus that a large proportion of the energetic motions in the actuated flow is associated with the large spanwise vortices shown in Fig. 14; in other words: the flow is more “organised”. Moreover, the increase in turbulence energy, observed in Fig. 8 when the synthetic jet is introduced, is primarily due to an increase in the fraction of turbulence energy associated with the largest scales. Similar observations have been made by Oster and Wygnanski [19], whose spectral analysis of a perturbed shear layer indicated that the energy associated with the large scales increased, while the energy of the smaller scales decreased.

**Table 3** List of  $q, m$ , percentage of total energy and eigenvalue for the first four modes in the baseline and synthetic-jet cases

Mode, $n$	Baseline				Synthetic-jet			
	$q$	$m$	$E_n/E_{\text{tot}}(\%)$	$\lambda$	$q$	$m$	$E_n/E_{\text{tot}}(\%)$	$\lambda$
1	1	1	4.76%	0.00024154	1	1	7.49%	0.00053419
2	2	1	2.62%	0.00013287	1	0	6.93%	0.00049472
3	3	1	1.88%	0.00009587	2	0	6.88%	0.00049057
4	4	1	1.69%	0.00008575	2	1	6.1%	0.00043535

The upper four plots in Fig. 16 show iso-surfaces of the first four most energetic POD eigenvectors of the streamwise-velocity component. The first two POD modes of the baseline flow in Fig. 16 are associated with large streamwise vortices downstream of separation. These vortices play a major role in the mixing process that dictates the extent of the recirculation bubble. A question that might be posed is whether the box size unduly constrains the streamwise structures and whether an increase in the box size would change the spanwise distance between two consecutive structures. This question remains open at the time of writing, but it is noted that the spanwise box of the present simulations is larger than that used in previous studies (see Table 2). In any event, RANS computations cannot resolve these streamwise vortices, and this may be a major reason for the excessively long recirculation regions observed to be predicted with RANS models (Rumsey et al. [23], Thiele and Jakirlić [31]). The iso-surfaces of the third and fourth modes show distinctly three-dimensional features and are representative of smaller-scale structures in the separated shear layer.

The lower four plots in Fig. 16 show iso-surfaces of the four most energetic POD modes of the streamwise-velocity component for the controlled case. An intriguing, perhaps counter-intuitive, observation is that the most energetic mode does not display features reflecting the strong spanwise vortices that are associated with the spanwise-uniform jet injection. Rather, the first mode indicates that the streamwise elongated features seen in Fig. 16, although somewhat disrupted by the injection, continue to dominate the structure, reflecting the dominant mixing process. It is only modes 2 and 3 that the footprint of the injection process via the distinct spanwise-uniform structures. One defensible interpretation of this behaviour is that the jet actuation is not “optimal”, either in strength or frequency or both, in so far as the primary mixing process of the separated baseline flow continues to dictate the behaviour in the controlled case. In fact, in Greenblatt et al. [9]  $F^+$  and  $C_\mu$  were chosen so that actuation would not completely remove the separation bubble in the mean, thus making the flow more challenging to its computational resolution. What is perhaps desirable is, thus, a modification of the injection parameters to an extent at which the mixing is more strongly dominated by the disturbances introduced by the injected jets. On the other hand, Table 3 shows that modes 1 to 4 have very similar amounts of energy associated with them. Therefore, even slight departures from full convergence in the POD analysis can have a material influence on the precise order of the modes. Nonetheless, the analysis shows, without ambiguity, that the injection strengthens the large-scale streamwise-elongated features in Fig. 16.

Figures 18 and 19 serve two purposes: first, they illustrate the temporal behaviour in the separation region for both cases; and second, they demonstrate how well the flow can be reconstructed from the first few POD modes. The latter is an important issue, in view of the fact that the energy content of the first few modes is a relatively small proportion of the total. While it is shown in Avdis [2] that more than 100 modes need to be accounted for to recover 50% of the energy of the baseline flow, it is demonstrated here that very few modes suffice to reconstruct a state that contains the most important features of interest. The figures record the time-variation of the streamwise velocity (or modal proportions thereof) along a streamwise-oriented line in the plane bisecting the spanwise slab and lying very close to the wall. The contours show only negative streamwise velocity, i.e. white areas identify attached flow, while darker areas indicate reverse flows.

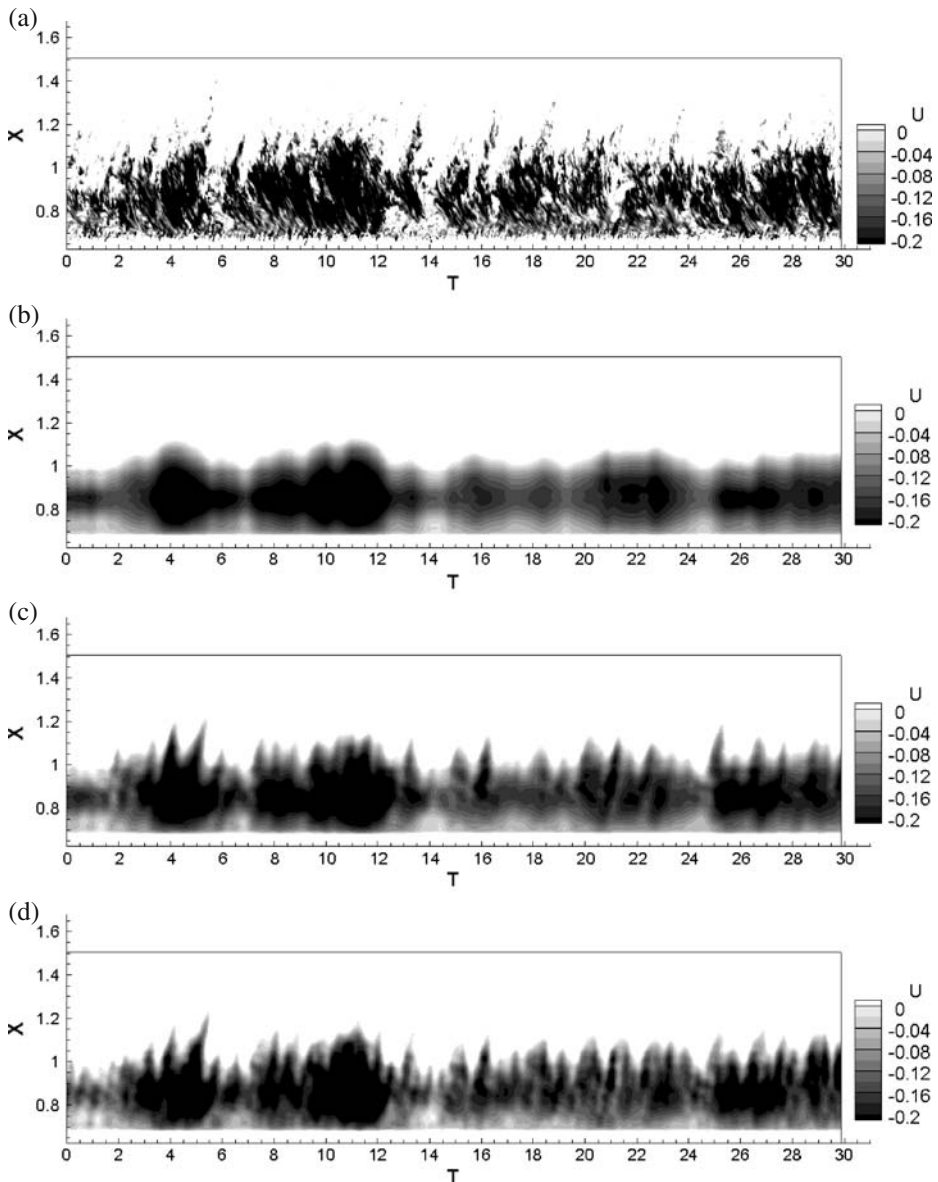


**Fig. 18** Space-time plot for one particular line extracted for the baseline case. The line is located at mid-span, in the first row of cells away from the wall and along the  $x$ -axis. This shows the evolution in time of the separated region, for **a** the original flow field, and **b** the flow field reconstructed using the first 2 most energetic modes, **c** the first 8 and **d** the first 16 modes

Figure 18 shows the behaviour of the separated region for the baseline case, with the top giving the actual velocity while lower plots provide reconstructions with 2, 8 and 16 POD modes. It is recalled that the time-mean reattachment position is at  $x/C = 1.08$ . The reattachment process appears to be highly non-periodic. An



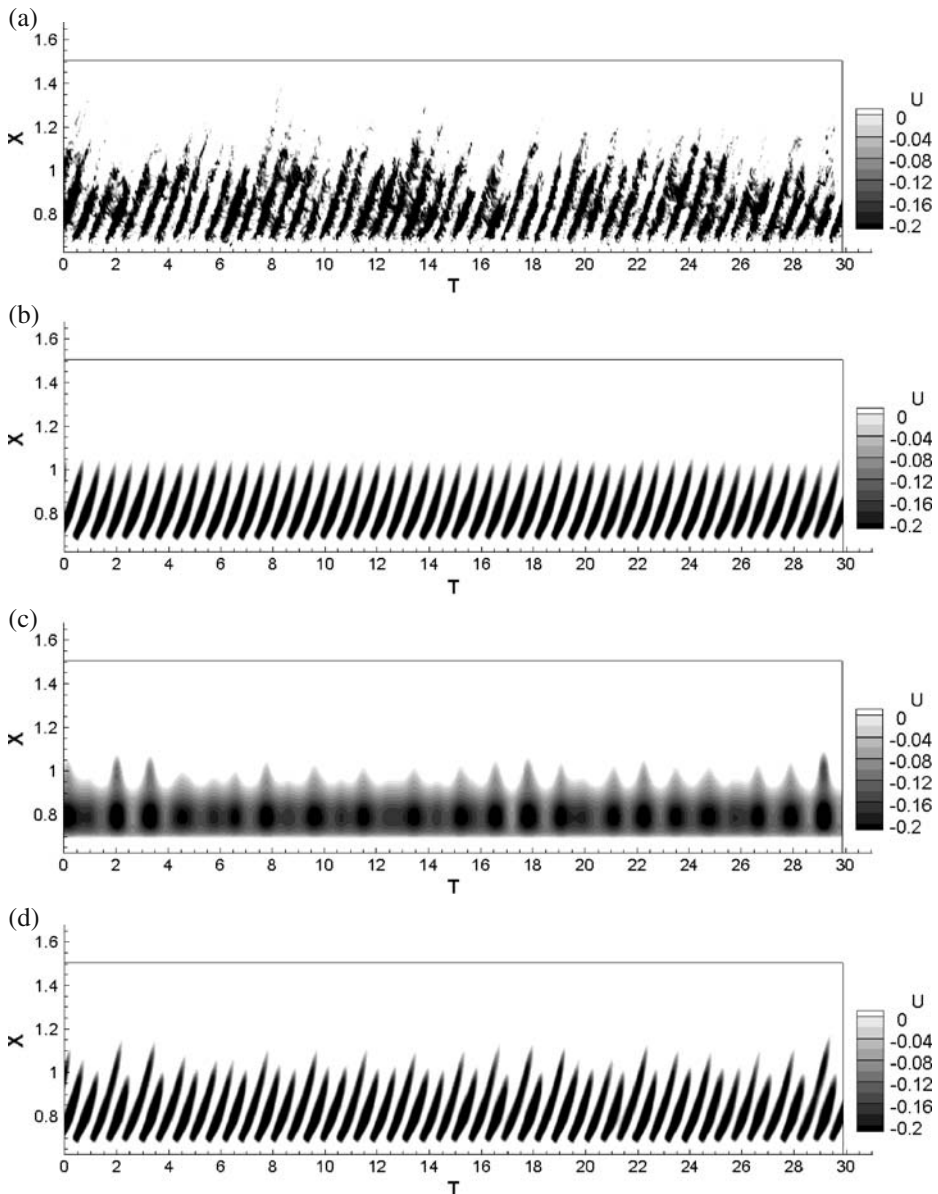


**Fig. 19** Space-time plot (same as Fig. 18 with synthetic jet. **a** Original flow field, and flow field reconstructed using **b** modes 2 and 3, **c** modes 1 and 4 and **d** mode 1 to 4

intriguing feature is the crescent-like shape of the contours, with symmetry at around  $x/C = 0.9$ . The interpretation of this feature is that there are frequently recurring periods in which regions of reverse flow on either side of  $x/C = 0.9$  are separated by a region of positive flow around this  $x$ -location. While the origin of this behaviour is unclear, it is conceivably connected to the presence of Kelvin-Helmholtz vortices in the separated shear layer, which can be perceived as provoking the impingement on



the wall of alternate regions of negative and positive velocity fluctuations. However, Fig. 7 does not reveal any obvious large-scale structures in the flow. A second useful observation is that the reconstruction of the flow field using the first two most energetic POD modes, identified as elongated streamwise vortices, Fig. 18b, has a very similar shape to the full field. Thus, the dynamics of the separation region is reasonably well described by the first two modes, which only represent 12% of the total fluctuating energy. Including further modes, (c) and (d), only refines the structure achieved with the first two modes, adding small-scale features. Hence, it may be asserted that much of the dynamics of the separation are driven by the streamwise-elongated structures seen in Fig. 16, which are highly non-periodic, as is evident from Fig. 17.

A radically different scenario is presented in Fig. 19 which relates to the actuated flow. In this case, injection leads to the formation of large vortical structures, as seen in Figs. 7 and 14. The traces of these structures are very distinct in Fig. 19a: separation (or reattachment) is initiated at the injection location, and is then “convected” downstream (the black stripes are inclined to the right, indicating forward convection in time). At any instant, a white (positive velocity) region can co-exist with two black (negative velocity) areas, and this indicates the presence of more than one roller in the  $x$ -range included. However, it is noted, on the top full-data plot, that this process, solely associated with the injection, is not exactly reproduced for every injection cycle, and there are clearly large variations in the reattachment location (ranging from  $x = 0.9$  to  $x = 1.1$ ). The reconstruction with modes 2 and 3 only (Fig. 19b) shows that the regular pattern in the actual flow is associated with the injection process, and that this process is very regular in time. Modes 1 and 4 (Fig. 19c), on the other hand, are not directly related to the control, but are linked to the streamwise elongated structure observed in the baseline case. Indeed, using these two modes alone, the reconstructed flow field appear to be always separated, but the reattachment point varies in time. The combination of the modes 1–4 leads to a much more realistic representation of the full process (Fig. 19d), with the reattachment point varying in time in a manner very similar to that of the actual flow. Indeed, for this particular case, the dynamics of the separation region can be represented with excellent accuracy by the first four initial modes. A final point to make in respect of this case is that the periods of injection, (modes 2,3), and the period of modulation, (modes 1,4), are very different: there are 48 jet periods recorded in the analysis, while there are 28 oscillations on the time-coefficients for modes 1 and 4 (Fig. 17b). This is the reason for the “beating” seen especially well in the reconstruction with all four modes in Fig. 19d).

## 5 Conclusions

In terms of agreement with the measurements, the simulations may be claimed to represent the experimental observations fairly well, especially in respect of the mean separation and reattachment locations and velocity profiles. The simulations predict a reduction of 30% in the streamwise extent of the bubble length, relative to the baseline case, compared to 28% in the experiment. This reduction reflects an increase in the turbulence activity associated with extra straining, as well as the added effects arising from periodic flapping when the synthetic jet is activated. It is shown

that the large vortical structures provoked by the injection and associated with the flapping are well captured by the simulation. Spectra provide indications that the receptivity of the flow to the periodic excitation is high due to the frequency of the injection being consonant with the flapping instability mode in the baseline flow. The simulations generally tend to over-estimate the Reynolds stresses in the separated shear layer, a behaviour which is opposite to that observed in RANS computations. This excess is compatible with the observation that the predicted thickness of the separated shear layer is larger than the one measured. Hence, the strain rate is somewhat lower. An exception to this excessive turbulence prediction is the shear stress in the actuated flow. In this case, the predicted shear stress is too low, although the stress is maintained at an elevated value over a wide portion of the separated shear layer.

In the baseline flow, the POD analysis has revealed the existence of large energetic streamwise structures, presumed to reflect streamwise vortices, in the separated shear layer. Such structures, which RANS solutions do not resolve, tend to promote mixing in the flow, thus shortening the separated zone. Although the four leading modes of the POD analysis carry a relatively small proportion of the total energy of the flow, evidence is provided in respect of the near-wall behaviour of separation and reattachment that much of the dynamics can be captured with a few modes.

With the synthetic jet active, large spanwise vortices are observed, both in the actual flow and the low-order POD analysis. These enhance mixing and reflect the strong response of the shear-layer-flapping instability to excitation at  $F^+ = O(1)$ . The POD analysis for this case has shown, as expected, that two of the four most energetic POD modes are associated with the large spanwise vortices. Less expected is the observation that the first mode continues to reflect the presence of the streamwise-aligned structures in the actuated flow, but these become “clumpy”, suggesting a break-up that is caused by an interaction with the spanwise perturbation introduced by the jet-injection process. However, because the energy distribution across the first four modes is very flat, it is difficult to state with any degree of certainty whether the order of the modes, as presented, is correct. In any event, the POD analysis shows that the behaviour in the separated zone, while being dominated by the periodicity of the injected process, is modulated by processes (or strong modes) that are inherent in the flow, whether with or without actuation.

**Acknowledgement** The authors are grateful to Dr. G. Fishpool for implementing of the third-order variant of the Gear scheme into the present LES code.

## References

1. Amitay, M., Smith, D., Kibens, V., Parekh, D., Glezer, A.: Aerodynamic flow control over an unconventional airfoil using synthetic jet actuators. *AIAA J.* **39**, 361–370 (2001)
2. Avdis, A.: Large Eddy simulation of synthetic jets in the context of flow control. Ph.D. thesis, Imperial College London, University of London (2008)
3. Dandois, J., Garnier, E., Sagaut, P.: Numerical simulation of active separation control by a synthetic jet. *J. Fluid Mech.* **574**, 25–58 (2007)
4. Deadroff, J.W.: A numerical study of three dimensional turbulent channel flow at large Reynolds numbers. *J. Fluid Mech.* **41**, 453–480 (1970)

5. Dejoan, A., Leschziner, M.: Large Eddy simulation of periodically perturbed separated flow over a backward-facing step. *Int. J. Heat Fluid Flow* **25**, 581–592 (2004)
6. Fishpool, G.M., Aydis, A., Leschziner, M.A.: Identification and removal of numerical instability components in low-order LES schemes. In: ERCOFTAC ETMM7 conference, Cyprus 2008 (2008)
7. Germano, M., Piomelli, U., Moin, P., Cabot, W.H.: A dynamic subgrid-scale eddy viscosity model. *Phys. Fluids* **3**(7), 1760–1765 (1991)
8. Gilarranz, J., Traub, L., Rediniotis, O.: A new class of synthetic jet actuators-part II: application to flow separation and control. *J. Fluids Eng.* **127**, 377–387 (2005)
9. Greenblatt, D., Paschal, K.B., Yao, C.-S., Harris, J., Schaeffler, N., Washburn, A.: Experimental investigation of separation control. Part 1: baseline and steady suction. *AIAA J.* **44**(12), 2820–2830 (2006)
10. Greenblatt, D., Paschal, K.B., Yao, C.-S., Harris, J.: Experimental investigation of separation control. Part 2: zero mass-flux oscillatory blowing. *AIAA J.* **44**(12), 2831–2845 (2006)
11. Holmes, P., Lumley, J.L., Berkooz, G.: *Turbulence, Coherent Structures, Dynamical Systems and Symmetry*. Cambridge University Press, Cambridge (1996)
12. Krishnan, V., Squires, K., Forsythe, J.: Prediction of separated flow characteristics over a hump. *AIAA J.* **44**(2), 252–262 (2006)
13. Launder, B., Sharma, B.: Application of the energy-dissipation model of turbulence to the calculation of flow near a spinning disc. *Lett. Heat Mass Transf.* **1**(2), 131–137 (1974)
14. Lilly, D.K.: A proposed modification of the Germano subgrid-scale closure method. *Phys. Fluids A* **4**(3), 633–635 (1992)
15. Lund, T.S., Xiaohua, W., Squires, K.D.: Generation of turbulent inflow data for spatially-developing boundary layer simulations. *J. Comput. Phys.* **140**, 233–258 (1998)
16. Menter, F.R.: Two-equation Eddy-viscosity turbulence models for engineering applications. *AIAA J.* **32**(8), 1598–1605 (1994)
17. Morgan, P.E., Rizzetta, D.P., Visbal, M.R.: Large-Eddy simulation of separation control for flow over a wall-mounted hump. *AIAA J.* **45**(11), 2643–2660 (2007)
18. Nishri, B., Wygnanski, I.: Effects of periodic excitation on turbulent flow separation from a flap. *AIAA J.* **36**(4), 547–556 (1998)
19. Oster, D., Wygnanski, I.: The forced mixing layer between parallel streams. *J. Fluid Mech.* **123**, 91–130 (1982)
20. Parekh, D., Palaniswamy, S., Goldberg, U.: Numerical simulation of separation control via synthetic jets. *AIAA paper* 2002–3167 (2002)
21. Pauley, L., Moin, P., Reynolds, W.: The structure of two-dimensional separation. *J. Fluid Mech.* **220**, 397–411 (1990)
22. Rhie, C.M., Chow, W.L.: Numerical study of the turbulent flow past an airfoil with trailing edge separation. *AIAA J.* **21**, 1525–1532 (1983)
23. Rumsey, C., Gatski, T., Sellers, L., Vatsa, N., Viken, S.: Summary of the 2004 computational fluid dynamics validation workshop on synthetic jets. *AIAA J.* **44**(2), 194–207 (2006)
24. Šarić, S., Jakirlić, S., Djugum, A., Tropea, C.: Computational analysis of locally forced flow over a wall-mounted hump at high-Re number. *Int. J. Heat Fluid Flow* **27**, 707–720 (2006)
25. Seifert, A., Darabi, A., Wygnanski, I.: Delay of airfoil stall by periodic excitation. *J. Aircr.* **33**, 691–698 (1996)
26. Sirovich, L., Ball, K.S., Keefe, L.R.: Plane waves and structures in turbulence channel flow. *Phys. Fluids A* **2**, 2217–2226 (1990)
27. Smagorinsky, J.: General circulation experiment with the primitive equations. *Mon. Weather Rev.* **91**(3), 99–164 (1963)
28. Spalart, P., Allmaras, S.: A one-equation turbulence model for aerodynamic flows. *La Recherche Aéronautique* **1**, 5–21 (1994)
29. Temmerman, L.: Large Eddy simulation of separating flows from curved surfaces. Ph.D. thesis, Queen Mary College, University of London (2004)
30. Tessicini, F., Temmerman, L., Leschziner, M.: Approximate near-wall treatments based on zonal and hybrid RANS-LES methods for LES at high Reynolds numbers. *Int. J. Heat Fluid Flow* **27**, 789–799 (2006)
31. Thiele, F., Jakirlić, S.: Meeting report on “Refined Turbulence Modelling: 12th ERCOFTAC/IAHR/COST Workshop, Berlin, October 12–13, 2006”, *ERCOFTAC Bulletin*, No. 75, pp. 5–10 (2007)
32. Werner, H., Wengle, H.: Large-eddy simulation of turbulent flow over and around a cube in a plate channel. 8th Symposium on Turbulent Shear Flows. Springer, New York (1991)

33. Yoshioka, S., Shinnosuke, O., Masuda, S.: Organised vortex motion in periodically perturbed turbulent separated flow over a backward-facing step. *Int. J. Heat Fluid Flow* **22**, 301–307 (2001)
34. You, D., Moin, P.: Large-eddy simulation of flow separation over an airfoil with synthetic jet control. *Center for Turbulence Research Annual Research Briefs*, 337–346 (2006)
35. You, D., Wang, M., Moin, P.: Large-eddy simulation of flow over a wall-mounted hump with separation control. *AIAA J.* **44**(11), 2571–2577 (2006)